ADVANCED MATERIALS INTERFACES
www.advmatinterfaces.de

SnO_2-SiO_2 1D Core-Shell Nanowires Heterostructures for Selective Hydrogen Sensing

Muhammad Hamid Raza, Navpreet Kaur, Elisabetta Comini, and Nicola Pinna**

SnO_2 is one of the most employed *n*-type semiconducting metal oxide in chemo-resistive gas-sensing although it presents serious limitations due to a low selectivity. Herein, the authors introduce 1D SnO_2-SiO_2 core-shell nanowires (CSNWs). The amorphous SiO_2-shell layer with varying thicknesses (1.8–10.5 nm) is grown onto the SnO_2 nanowires (NWs) by atomic layer deposition (ALD). SiO_2-coated SnO_2 CSNWs show a dramatic improvement of the selectivity towards hydrogen. Moreover, the sensing-response is strongly correlated to the thickness of the SiO_2-shell and the working temperature. The SnO_2-SiO_2 CSNWs sensor with a 4.8-nm SiO_2 shell thickness exhibits the best selectivity and sensitivity, having ca. 7-fold higher response toward hydrogen compared to bare-SnO_2 NWs. The selectivity and enhanced sensing-response are related to the masking effect of the SiO_2 shell and an increase in the width of the electron-depletion-layer due to a strong electronic coupling between the SnO_2 core and SiO_2 coating, respectively.

1. Introduction

Hydrogen is extensively used in numerous fields such as aerospace, chemical industry, fuel cells, electronics, and civil engineering.[1] Taking into account the very low and wide flammable and explosive range of H_2 concentrations (4–75%), and its colorless and odorless properties, the management and safety of hydrogen raise a demanding challenge.[2] Therefore, it is crucial to monitor hydrogen leakages at trace levels.[3]

SnO_2 is the most studied *n*-type semiconducting metal oxide (SMOX) employed in chemo-resistive gas-sensing, due to its wide band gap (3.6 eV at 300 K), low material cost, fast response, and stability.[4] However, gas sensors composed of SnO_2 and related materials are limited by their low selectivity, for example, interference with other reducing gases such as methane, ethanol, and carbon monoxide that prevents accurate hydrogen detection.[5] It has been demonstrated that SnO_2-based gas sensors show significant enhancement in their gas-sensing characteristics by combining SnO_2 with secondary-materials, for instance by doping,[6] surface modification with noble metals catalysts (Pd, Au, Ag, Pt)[4b,7] and metal oxides (ZnO, In_2O_3, NiO).[5,8] Moreover, SMOX loaded with other materials can exhibit improved sensing characteristics due to modified transducer/receptor functions. Finally, nanoscale heterojunctions can further increase the gas-sensing responses due to the Fermi-level effect.[9]

One of the efficient methods to enhance selectivity of chemo-resistive gas sensors is to use a catalytic membrane on top of the core-materials.[10] For example, it is possible by using platinum, palladium, and nickel membranes to enhance the hydrogen and ethanol selectivity of a sensor in presence of other interfering gases.[11] Additionally, some metal organic frameworks (MOFs) materials such as zeolitic imidazolate frameworks (ZIF-67 and ZIF-8) have been reported to act as molecular sieves to enhance the selectivity of gas-sensors.[12] Especially, high response-signals were recorded for low concentration of H_2, whereas no significant response toward other interfering gases such as benzene, toluene, acetone, and ethanol were detected.[12a] On the other hand, metal organic frameworks (MOFs) are not stable at the typical operating temperature of SnO_2-based gas sensors (around 400 °C). Likewise, the use of a SiO_2 amorphous film onto an active substrate (mostly SnO_2) has also been reported to improve the selectivity for hydrogen sensing.[10b,13] In these sensors, the amorphous SiO_2 films apparently acts as "molecular-sieves", effectively decreasing the diffusion of some gases having larger molecular sizes than H_2, leading to an improved selectivity to H_2.[14]

SiO_2 coatings onto the SMOX are typically produced by chemical vapor deposition (CVD) or soft-chemistry approaches such as the sol-gel process using different silanes such as ethoxysilanes, hexamethyldisiloxane (HMDS), triethoxymethylsilane (TEMS), ethoxy-trimethylsilane (ETMS), and dirthoxydimethylsilane (DEMS) by dip- or spin-coating.[10b,14,15] Even though an improvement in the selectivity towards H_2 detection has been reported by using SiO_2–SnO_2 based materials, most of these reported

M. H. Raza, Prof. N. Pinna
Institut für Chemie and IRIS Adlershof
Humboldt-Universität zu Berlin
Brook-Taylor-Str. 2, 12489 Berlin, Germany
E-mail: nicola.pinna@hu-berlin.de
Dr. N. Kaur, Prof. E. Comini
Sensor Lab
Department of Information Engineering
University of Brescia
Via Valotti 9, Brescia 25133, Italy
E-mail: elisabetta.comini@unibs.it

The ORCID identification number(s) for the author(s) of this article can be found under https://doi.org/10.1002/admi.202100939.

DOI: 10.1002/admi.202100939

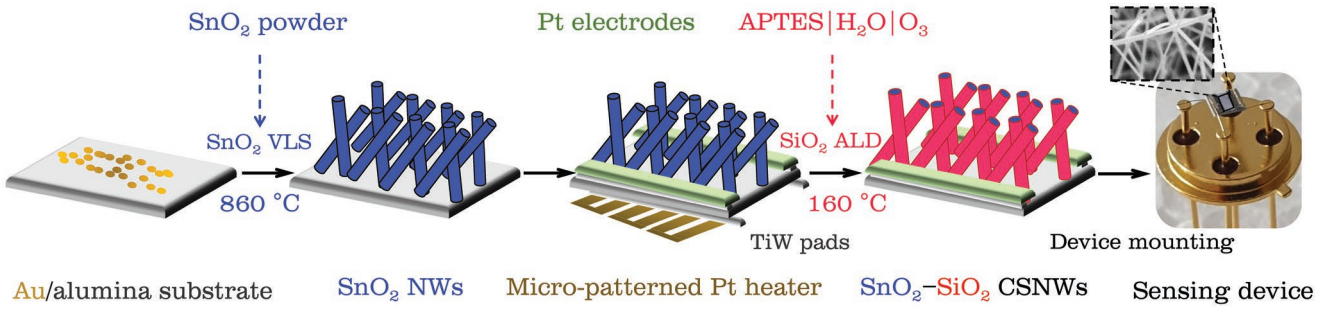

Scheme 1. Synthesis of the SnO_2-SiO_2/*N* CSNWs and fabrication of the gas sensing devices.

nanomaterials lack in a fine control over the properties of the SiO_2 layer in terms of homogeneity, conformability, and thickness.[14] As a matter of fact, only with a precise control of the SiO_2 coating, it would be possible to address fundamental questions like: i) how the SiO_2-shell layer acts as a molecular sieve; ii) how the thickness of the SiO_2 coating influences the sensitivity and selectivity and ultimately leads to an improvement in the sensing performance; and iii) what is the transducing mechanism of the heterostructures. Hence, only well-defined hierarchical nanostructures can be used to propose a clear structure–properties relationship.[5,9b,15d,16]

The choice of the active sensing material where such a masking layer can be applied is another significant factor. In recent years, due to their high surface-to-volume ratio and distinctive morphology, numerous 1D nanostructures (for example; nanowires, nanorods, and nanobelts) have been synthesized and studied as the active material in state-of-the-art SMOX based gas-sensors.[7a,17] These 1D NWs provide a sizeable amount of surface active sites for the adsorption of gaseous species due to their high surface area.[18] For examples, one of our recent study has shown that core-shell heterostructures based on SnO_2-NiO exhibited enhanced sensing properties towards hydrogen as compared to bare-SnO_2 nanowires.[5] In that case, the enhanced sensing-response after the NiO-coatings was assigned to the creation of a *p*–*n* heterojunction and to the modulation of the space charge region. Moreover, it was demonstrated that the sensing-response was related to the NiO-shell thickness.[5] Therefore, also in this study 1D SnO_2 nanowires (NWs) are chosen as the model material to study the role of the SiO_2-coating thickness.

In this study, we describe the fabrication of well-defined hierarchical 1D SnO_2 (core)/SiO_2 (shell) core-shell nanowires (CSNWs) with varying shell thicknesses directly onto the sensing device using vapor–liquid–solid (VLS) and atomic layer deposition (ALD) techniques. Since it is crucial to control the size of the nanowires and the thickness (at a level of a few nanometers) of the shell layer deposited onto the core substrate, ALD was selected as a deposition technique in this study. ALD shows an Ångström-level control over the thickness of the shell layer due to the fact that the technique is based on self-terminated surface reactions.[19] Besides, ALD can develop reproducible, homogenous, and conformal coatings of high-aspect ratio nanostructured substrates at comparatively lower temperatures retaining the fundamental characteristics of the base-materials.[20] The gas sensing characteristics of the SnO_2-SiO_2/*N* CSNWs are studied as a function of the SiO_2-shell thickness allowing to elucidate the underlying gas-sensing mechanism. To the best of the author's knowledge, this is the first report where the role of the amorphous SiO_2 shell layer conformally coated onto 1D SnO_2 nanostructures has been studied by designing structurally well-defined hierarchical heterostructures with varying thickness of the SiO_2 films. The material synthesis and device fabrication process are presented in **Scheme 1**.

2. Results and Discussion

2.1. Structural Characterization

Figure S1a, Supporting Information, shows bright-field (BF) TEM image of non-coated SnO_2 NWs. The as-synthesized SnO_2 NWs are relatively homogeneous showing nanowires like morphology with diameters ranging from 50–70 nm. Moreover, scanning electron microscopy (SEM) micrographs (for bare SnO_2 NWs and SnO_2-SiO_2/130 CSNWs) in Figure S1b–d, Supporting Information, further confirm that the pristine SnO_2 NWs are well-calibrated in size and diameter, and homogeneously dispersed onto the alumina substrate. After the ALD process, the SEM images show a well-retained morphology of the SnO_2 NWs.

The morphology and microstructure of all the samples were investigated by high-resolution transmission electron microscopy (HRTEM). Bright-field high-resolution transmission electron microscopy (BF-HRTEM) image for an isolated bare-SnO_2 nanowire is shown in **Figure 1**a. The corresponding selected area electron diffraction (SAED) (Figure 1b) shows reflections corresponding to a single crystal of cassiterite (rutile-type structure) aligned along the $[\bar{1}00]$ zone axis, where the corresponding reflections are marked accordingly (ICDD 00-001-0625). The BF-TEM micrographs of isolated SiO_2-coated SnO_2 NWs (SnO_2-SiO_2/*N*) and the respective magnified-views (cf. insets) show that the SnO_2 NWs are conformally coated with a continuous film of SiO_2 confirming the hierarchical core-shell like heterostructure (Figure 1c–h). The average thickness of the SiO_2 film measured from the TEM images are 1.8, 3.1, 4.8, 7.5, and 10.5 nm for 20, 40, 60, 90, and 130 ALD cycles, respectively (Table S1, Supporting Information). It can be seen that the thicknesses of the SiO_2 shell layers onto the SnO_2 nanowires are well-calibrated, and increased with increasing the number of SiO_2 ALD cycles. The plot of the thickness of SiO_2 as a function of the number of ALD cycles represents a good linearity (R^2 = 0.998) with a slope pointing to a growth per cycles (GPC) of 0.081 nm/cycle. The estimated thicknesses of the SiO_2 coatings as a function of the ALD cycles from the TEM images and by the ellipsometry are comparable, proving the saturation behavior for the ALD process on both substrates (Table S1 and Figure S2, Supporting Information). Figure 1i shows the SAED pattern corresponding to an isolated

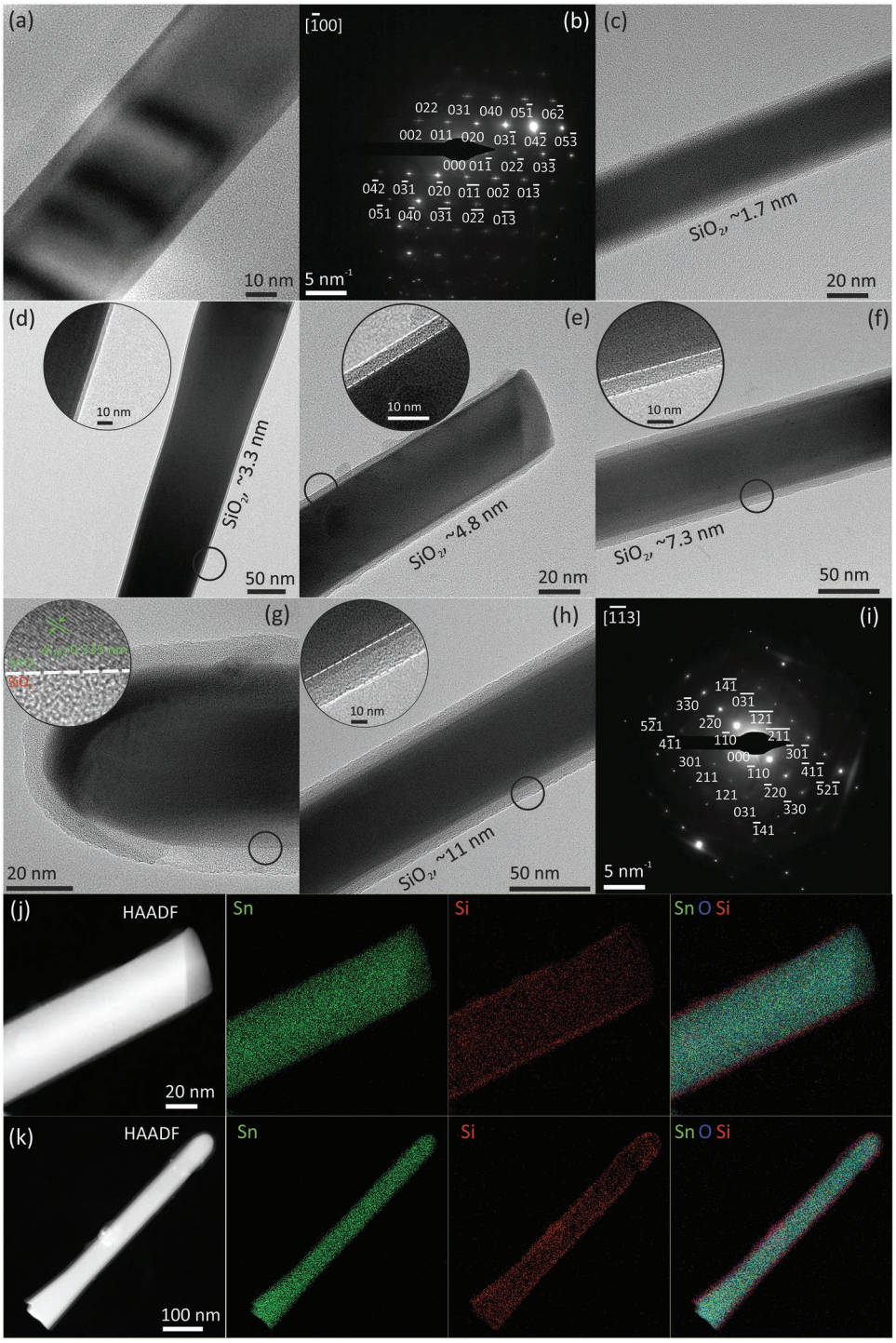

Figure 1. Bright-field high resolution transmission electron microscopy (BF-HRTEM) micrographs of bare-SnO_2: a) an isolated SnO_2 nanowire and b) the corresponding SAED pattern. BF-HRTEM micrographs for the isolated SnO_2-SiO_2/*N* CSNWs: c) SnO_2-SiO_2/20, d) SnO_2-SiO_2/40, e) SnO_2-SiO_2/60, f,g) SnO_2-SiO_2/90, h) SnO_2-SiO_2/130 and i) corresponding SAED pattern. HAADF-STEM images and the corresponding EDX elemental mappings for the j) SnO_2-SiO_2/60 and k) SnO_2-SiO_2/90 CSNWs. The insets in (d–h) show magnified view of the encircled areas in the corresponding micrographs.

SnO_2-SiO_2/130 CSNW in Figure 1h, which shows a single crystalline pattern for SnO_2, where the corresponding reflections marked correspond to [$\bar{1}$13] zone axis. Notably, other than the cassiterite phase of SnO_2, no additional reflections are present that can be indexed to ALD-deposited SiO_2. This implies that SnO_2 remained single crystalline after SiO_2 ALD, while the ALD-SiO_2 thin film is as expected amorphous.[20a] The magnified view in the inset in Figure 1g clearly demonstrates the presence of two distinctive

phases, that is, crystalline SnO_2-core and amorphous SiO_2-shell. The *d*-spacing of 0.335 nm in SnO_2 region can be assigned to the (110) plane of the SnO_2 cassiterite phase (Figure 1g).

The high-angle annular dark-field scanning transmission electron microscopy (HAADF-STEM) images for the SnO_2-SiO_2/*N* (*N*, 60 and 90) samples show a conformal and homogeneous coverage of the SnO_2 NWs with an amorphous SiO_2 thin film. This is consistent with the bright-field TEM images, where the phases of SnO_2 and SiO_2 can be identified easily due to their different *Z*-contrast (Figure 1j,k). The energy-dispersive X-ray spectroscopy (EDX) elemental mappings corresponding to the HAADF-STEM images show the presence of Si, Sn, and O atoms with a homogenous and conformal SiO_2 film onto the SnO_2 nanowires further confirming the CSNW-like heterostructures (Figure 1j,k). Figure S3, Supporting Information, shows the EDX spectra corresponding to the elemental mappings shown in Figure 1j,k for the SnO_2-SiO_2/60 and SnO_2-SiO_2/90 CSNWs.

2.2. Electrical Characteristics

To study the electrical behavior of the sensing devices and to assess the effect on the electrical conductance of the interface at SnO_2-base material and the SiO_2-shell, the baseline conductance of all of the bare-SnO_2 NWs and SiO_2-coated SnO_2 CSNWs samples were recorded in nitrogen and in air. Figure S4, Supporting Information, shows the baseline conductance of all the devices as a function of the temperature (RT-500 °C) under nitrogen. All the sensors show a monotonic increase in conductance with increasing the temperature from room-temperature to 500 °C, thereby confirming a dominant semiconducting behavior of the CSNWs heterostructures.[9b] Thus, the insulating nature of the SiO_2-shell layers did not alter the semiconducting behavior of the SnO_2 NWs. Noticeably, in these devices, because the electrodes are directly connected to the SnO_2 network before the SiO_2 ALD step, the insulating SiO_2-coating acts only as a surface modifier of the fabricated device. However, an effect due to the SiO_2 coating was also observed, as a matter of fact the electrical conductance decreased for all of the SnO_2-SiO_2/*N* CSNWs sensors as compared to the pristine SnO_2 NWs. Under nitrogen, it can be assumed that the modification of the acceptor states due to the chemisorption of oxygen species is negligible. Therefore, a drastic decrease in electrical conductance (or increase in resistance) would point to an electron-depletion-layer (EDL) at the interface of the SnO_2-core and SiO_2-shell layer similar to that has been demonstrated in the case of electronic coupling at SMOX–SMOX interfaces.[21] The conductance of the SnO_2 NWs samples decrease significantly (up to four orders of magnitude) depending on the thickness of the SiO_2 coating at a particular operating temperature (Figure S4, Supporting Information). This is attributed to an additional component of the resistance due to the extraction of electrons from the SnO_2 NWs conduction band by SiO_2.[22] Thus, a junction is formed at the SiO_2–SnO_2 interface,[15c,23] which introduced an electron-depletion-layer (EDL) at the SnO_2 surface (Scheme 2a,d see also discussion below).

In addition, the electrical conductance of all the sensors were recorded (in dry air) and these values were used as reference and baseline for the gas-sensing study. There is a clear difference in the baseline conductance (G_{air}) among pristine and SiO_2-coated SnO_2 NWs sensors (**Figure 2**a). As a matter of fact, the conductance of the SnO_2-SiO_2 CSNWs sensors in air decreased sharply with the increase of the SiO_2-shell thickness up to the ca. 4.8 nm. It is well known that the electrical conductance at a particular temperature is seriously affected by the concentration of absorbed oxygen species.[5,21b] A comparison of the baseline conductance of all of the pristine and SiO_2-coated SnO_2 NWs sensors in nitrogen to the same sensor in dry air shows that the conductance decreased with the introduction of dry air (baseline conductance values, Figure 2a). This shows that oxygen can diffuse through the SiO_2-shell to the SnO_2 NWs. On the other hand, the extent of the difference in conductance from nitrogen to dry air decreased for the samples with higher thickness (>4.8 nm), suggesting that a thicker SiO_2-shell film hinders the diffusion of oxygen species to the SnO_2 surface (Figure 2a). Likewise, the baseline-conductance of the SnO_2/SiO_2-*N* CSNWs sensors show a steep decline with increasing the SiO_2-shell layer thickness up to the thickness ca. 4.8 nm (SnO_2-SiO_2/60 CSNWs), and then it stayed at a similar value with further increasing the shell thicknesses (studied up to ca. 10.5 nm). Therefore, we can conclude that only at higher thicknesses (>5 nm), the SiO_2 coating impedes the diffusion of oxygen species to the SnO_2 NWs surfaces.

2.3. Gas Sensing Properties

The gas-sensing tests were performed for a series of SnO_2 NWs and SnO_2-SiO_2/*N* CSNWs devices in the presence of hydrogen gas and some interfering gases (namely; ethanol, acetone, CO, and H_2S) at different working temperatures in dry air (0% RH) and in a relative humid environment (40% RH). The isothermal electrical conductance transients recorded at 500 °C to different concentrations of H_2 (i.e., 50, 200, and 500 ppm) in dry air (RH 0%) and 40% of relative humidity (RH 40%) are presented in Figure 2b,c and Figure S5a, Supporting Information. As the hydrogen gas was introduced into the testing chamber, the electrical conductance of all the sensors increased, and shortly reached a maximum conductance value, followed by a recovery to their baseline as the hydrogen exposure was stopped (Figure 2b). This shows an *n*-type response typical of SnO_2-based SMOX gas-sensors. SnO_2 is a well-known non-stoichiometric SMOX showing *n*-type semiconducting behavior due to the presence of oxygen vacancies.[5] As described above (cf. electrical characteristics section), the presence of a SiO_2-shell did not affect the semiconducting behavior (*n*-type) of the SnO_2 NWs. Thus, the SnO_2-SiO_2/*N* CSNWs devices show a response due to the SnO_2-core in the CSNWs heterostructures and the electrons conduction path should be confined to the SnO_2-core, that is, along the conductive core-axis (cf. discussion below). Moreover, all the sensors show a dynamic reversible response, where the response towards H_2 increases with increasing the concentration in both dry air and in air with 40% RH (Figure 2b,c).

Figure 2d represents the sensing-response of the devices composed of bare-SnO_2 NWs and SnO_2-SiO_2/*N* CSNWs with different thicknesses of the SiO_2-films toward 200 ppm of H_2 in the temperature ranges 200–500 °C. Noticeably, the response of all the sensors increased with increasing the temperature and the SnO_2-SiO_2/*N* CSNWs sensing devices with a SiO_2 coating thinner or equal to 4.8 nm showed a higher response towards

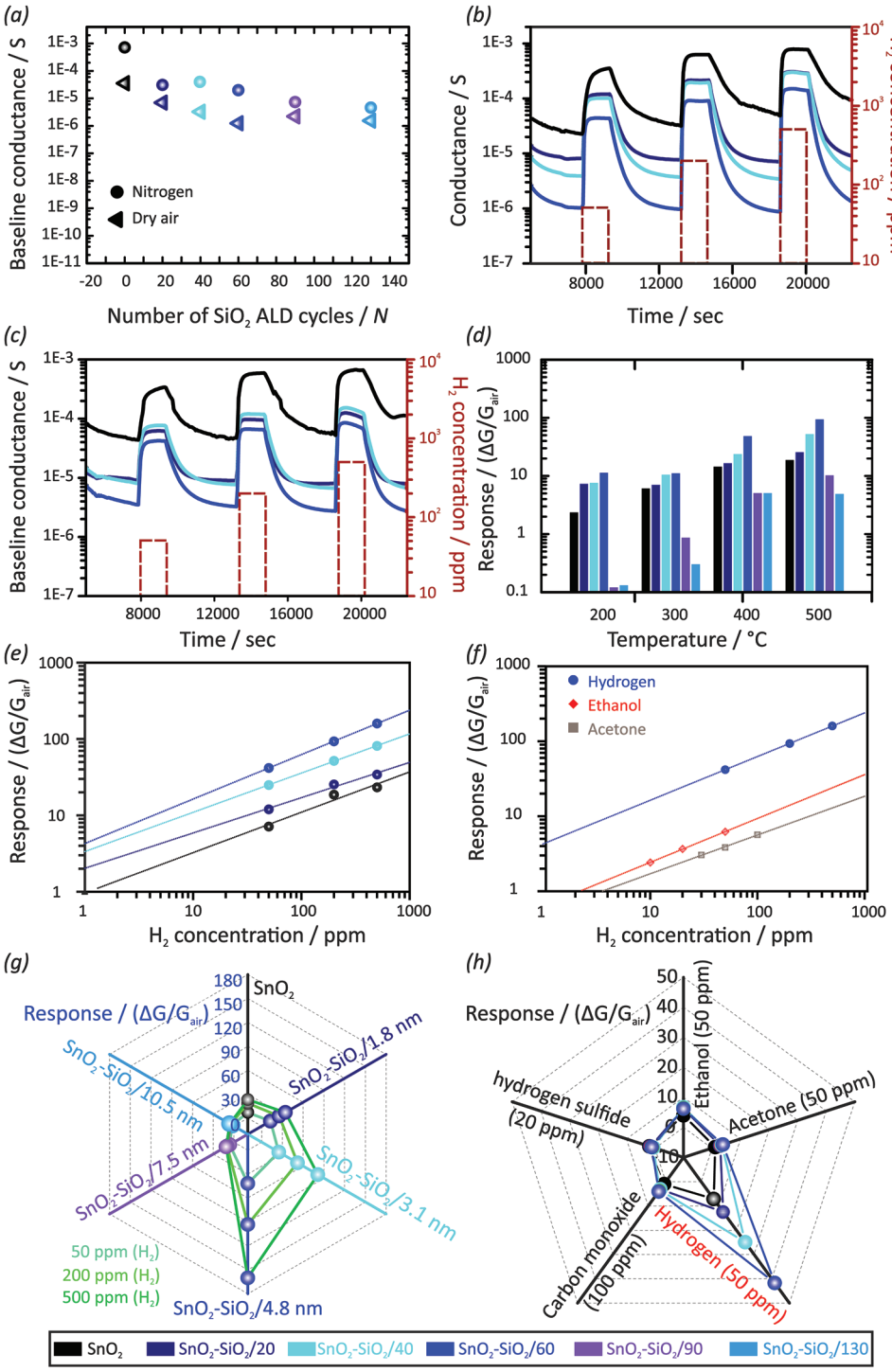

Figure 2. a) Baseline conductance of SiO_2-coated SnO_2 CSNWs (SnO_2-SiO_2/*N*) and bare-SnO_2 NWs sensors in dry air and in nitrogen at 500 °C. The response transient of the sensors composed of bare SnO_2 NWs and the SnO_2-SiO_2/*N* CSNWs at 500 °C to the different concentrations (50–500 ppm) of H_2, b) in dry air and c) in air with 40% RH. d) The response of the bare-SnO_2 NWs and the SnO_2-SiO_2/*N* CSNWs sensors toward H_2 (200 ppm) at different temperatures (200–500 °C). The power-law fits of the e) sensing-response versus different concentrations of hydrogen at 500 °C for the sensors fabricated with bare-SnO_2 NWs and various SnO_2/NiO-*X* CSNWs in dry air, and f) sensing-response versus different concentrations of hydrogen, acetone, and ethanol for the best performing sensor (SnO_2-SiO_2/60 CSNWs) at optimal working temperature of 500 °C. g) The response of the bare SnO_2 NWs and the SnO_2-SiO_2/*N* CSNWs sensors with different thicknesses of the SiO_2 amorphous films to hydrogen (i.e., 50, 200, and 500 ppm) at a temperature of 500 °C. h) Response of the SnO_2-SiO_2/*N* CSNWs and the bare-SnO_2 NWs sensors toward hydrogen (50 ppm) and common interfering gases, ethanol (50 ppm), carbon monoxide (100 ppm), acetone (50 ppm), and hydrogen sulfide (20 ppm) at 500 °C. The color code shown at the bottom of the figure is the same for all the panels. Part of the bare-SnO_2 NWs data are the same as in our earlier report.[5]

hydrogen compared to the reference (Figure 2d). This is due to the comparatively high thermal energy to overcome the activation energy barrier for the surface reactions and the selective H_2 diffusion to the SnO_2 surface across the SiO_2 coating, respectively.[24] The sensing response of the different sensors versus H_2 concentration at 500 °C (i.e., optimal working temperature) in dry air (0% RH) are shown in Figure 2e. The higher the concentration of hydrogen, the greater is the response of the sensors. The calibration curves, response versus H_2 concentration follow a power-law relation (in agreement with the Equation (7)) for SMOX-sensors, further confirming the absence of any saturation process.[5,18b] The sensors detection limit is calculated while taking into account the minimum response value of 1 in the fits of Equation (7). The values of different parameters calculated by the power-law fits are summarized in Table S2, Supporting Information. The best performing sensors show a detection-limit at parts-per-billion-level (0.1 ppm for both of the SnO_2-SiO_2/40 and SnO_2-SiO_2/60 CSNWs sensors) at 500 °C. Moreover, the SnO_2-SiO_2/60 CSNWs sensor shows a lower detection limit for hydrogen (0.1 ppm) as compared to ethanol (2.2 ppm) and acetone (3.8 ppm), cf. Figure 2f and Table S3, Supporting Information. It is important to point out that the SnO_2-SiO_2/*N* CSNWs sensors showed a good selectivity towards hydrogen together with a comparatively higher sensing-response than the bare-SnO_2 NWs both in dry air and in air with 40% RH. The response of all the fabricated sensors decreased with increasing the relative humidity (Figure S5b, Supporting Information). This decrease in the sensing-response in humid environment for SMOX gas sensors is due to the competition of the adsorption between water molecules and the analytes and is well documented.[5,18b] Figure 2g and Figure S5b, Supporting Information, compare the sensing response for the bare-SnO_2 NWs and SnO_2-SiO_2 CSNWs with different thickness of the SiO_2-shell layer, in dry air and in 40% RH, respectively. The SnO_2-SiO_2 CSNWs sensors with a shell thickness ≈1.8–4.8 nm show an enhanced sensitivity towards hydrogen compared to the bare-SnO_2 NWs sensors. Indeed, the SnO_2-SiO_2/60 CSNWs sensor shows a 6 to 7-fold increase in response than the non-coated SnO_2 NWs for all of the tested concentrations of hydrogen (50–500 ppm) at 500 °C cf. Figure 2g. In addition, among the SnO_2-SiO_2 /*N* CSNWs sensors, the sensing-response increased initially with increasing the SiO_2-shell thickness up-to the ca. 4.8 nm (i.e., for SnO_2-SiO_2/60 CSNWs), and then it decreased with further increasing the SiO_2-shell thickness. For example, the bare-SnO_2 NWs and SiO_2-coated SnO_2 CSNWs (SnO_2-SiO_2/*N*) sensors with 20, 40, 60, 90, and 130 ALD cycles show a response of 7, 13, 25, 42, 6, and 3 towards 50 ppm of hydrogen, respectively (Figure 2g). The SnO_2-SiO_2/60 CSNWs sensor shows the best response among all the sensors. This sensor revealed a distinguished response of 160 toward H_2 (500 ppm, i.e., approximately two-orders-of-magnitude less as compared to the explosive limit of hydrogen)[5] in dry air at 500 °C.

Figure 2h shows the response of the bare-SnO_2 NWs and SnO_2-SiO_2/*N* CSNWs to hydrogen and common interfering gases at 500 °C. The response towards H_2 greatly increases after SiO_2 coating. On the other hand, the response to acetone, ethanol, CO, and H_2S is less significant and is almost not affected by the SiO_2 coating. The SnO_2-SiO_2/60 CSNWs, the best performing sensor, show a response of 6.2, 3.8, 4, 1, and 42 toward ethanol (50 ppm), acetone (50 ppm), CO (100 ppm), H_2S (20 ppm), and hydrogen (50 ppm), respectively (Figure 2h). Clearly, the SnO_2-SiO_2/*N* CSNWs sensors exhibit a negligible cross-sensitivity to the selected interfering gases making them appropriate for real time hydrogen-detection applications. The comparison of our sensors to some state-of-the-art SnO_2-based nanostructures for the selective detection of hydrogen (Table S4, Supporting Information) demonstrate that our heterostructures positively compare to previously reported materials.

2.4. Gas Sensing Mechanism and Discussion

Scheme 2 shows the different regions involved in the transduction mechanism for both the bare-SnO_2 NWs and the SnO_2-SiO_2/*N* CSNWs. A detailed sensing mechanism for the SnO_2 NWs has already been described in our earlier report.[5] Briefly, the sensor signal is based on the charge transfer as a result of redox reactions between the chemisorbed oxygen species (O^{2-}, O_2^-, and O^-) and the analytes at the surface of the SMOX, which mainly induce a change in the electrical resistance of the device. In air, oxygen species adsorbed onto the SnO_2 surface withdraw electrons from the conduction band of the SMOX resulting in an electron-depletion layer (EDL) near the surface (Equations (1) and (2)). This creates a surface potential, that is, a Schottky barrier resulting in an upward band bending. Another potential barrier (back-to-back Schottky barrier) is created in case of a SnO_2 NWs network due to the contacts between the depleted surface of the nanowires with each other, that is, at the SnO_2–SnO_2 junction (Scheme 2a,b).[18b,c,25]

When an analyte such as hydrogen (a reducing-gas) is introduced, it is oxidized during the reaction with the adsorbed oxygen species at the SnO_2 surface by donating electrons back to the conduction band of the SnO_2, thus accordingly decreasing the electron depletion region (decreasing the potential barrier height), Equations (3) and (4). This results in an increase in the width of the conduction channel and therefore to an increase of the electrical conductance of the sensor (Scheme 2c). Hence, the change in resistance of the device fabricated with bare-SnO_2 NWs is a combination of a series of resistances, that is, modification of the potential barrier height due to back-to-back SnO_2-SnO_2 homojunction and the change of the surface depletion region.[9b,26] Importantly, due to the small size and diameter of the SnO_2 NWs, these changes in the electrical signals become significant because the space-charge region participates significantly to the resistance modulation together with the potential barrier at back-to-back homojunction.[5,9b,27]

$$O_{2(gas)} + 2e^- (SnO_2)_{(CB)} \rightleftarrows 2O^-_{ads} (SnO_2) \quad (1)$$

$$O_{2(gas)} + 2e^- (SnO_2)_{(CB)} \rightleftarrows O^-_{2\,ads} (SnO_2) \quad (2)$$

$$2H_{2(gas)} + O^-_{2,ads} \rightarrow 2H_2O_{(des)} \uparrow + e^- (SnO_2)_{(CB)} \quad (3)$$

$$H_{2(gas)} + O^-_{(ads)} (SnO_2) \rightarrow H_2O_{(des)} \uparrow + e^- (SnO_2)_{(CB)} \quad (4)$$

In the SiO_2 coated SnO_2 CSNWs, an additional heterojunction is introduced between the SiO_2-shell and the SnO_2-core, thereby narrowing the conduction channel along the SnO_2-core and increasing the resistance of the whole system.[22,23]

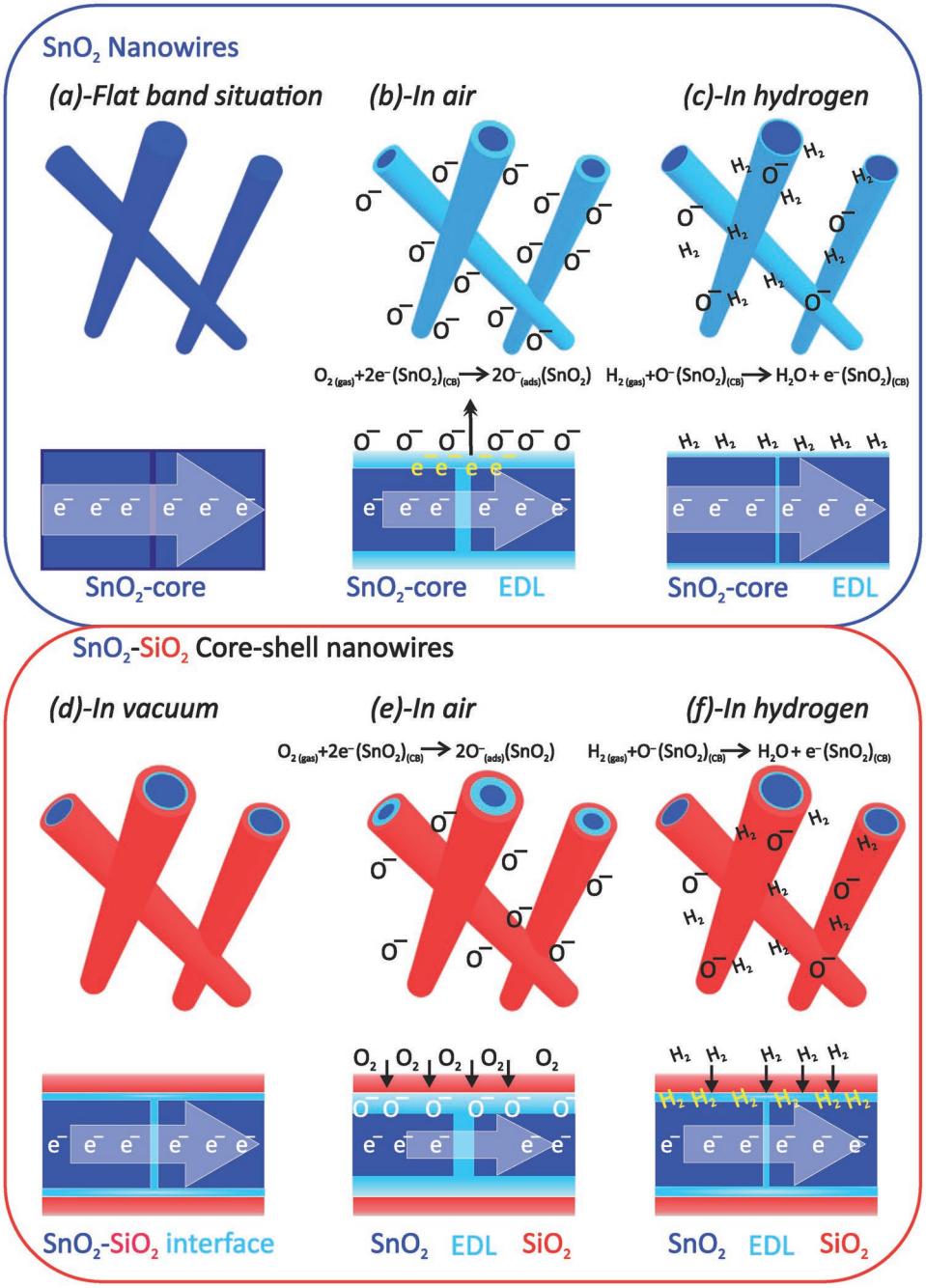

Scheme 2. A presentation of the proposed sensing mechanism and effective conduction channel for the bare and SiO_2-coated SnO_2 core-shell nanowires. a–c) represents bare-SnO_2 NWs: a) in vacuum (flat-band situation), b) in air, the chemisorbed oxygen species withdrawing electrons from the conduction band of SnO_2 by creating an electron depletion layer, thus narrowing the conduction channel and enhancing the barrier height at the surface and at the back-to-back junctions, c) in H_2, the H_2 adsorbed onto the SnO_2 surface donating electrons back to the depleted surfaces, reducing the barrier height along with expanding the conduction channel. d–f) SnO_2-SiO_2 CSNWs: d) in vacuum, where a SnO_2-SiO_2 junction is formed by creating the electron-depletion-layer (EDL) at the interface of the two materials (indeed the conduction channel became narrow as compared to the pristine SnO_2 NWs), e) in air, as the chemisorbed oxygen species withdraw electrons from the conduction band of SnO_2, thus broadening the EDL at the interface with further narrowing the charge conduction channel, f) in hydrogen, amorphous SiO_2-shell layer acts as a selective filter for hydrogen, the hydrogen species can diffuse at the SnO_2 surface and oxidize donating electrons back to the conduction band of SnO_2, thus shrinking the EDL and expanding the conduction channel. Figure S6, Supporting Information, shows the energy band diagram for the SnO_2-SiO_2 heterojunction interface in air and hydrogen.

Importantly, due to the insulating nature of SiO_2 the electron conduction path is confined to the SnO_2-core, that is, along the conductive core-axis (Scheme 2d).[5]

When the SiO_2-coated SnO_2 CSNWs (SnO_2-SiO_2) sensor is exposed to air, oxygen can diffuse through the thin SiO_2-shell to the SnO_2 core and chemisorbs by capturing electrons from

the conduction band of the SnO_2 (*n*-type SMOX). Thus the width of the EDL increases when the sensor is exposed to air narrowing the conduction channel (Scheme 2e and Figure S6, Supporting Information). The SiO_2-shell acts as a molecular sieve where the analyte has to diffuse through the SiO_2 layer to react at the SnO_2 surface. Therefore, the density of the film, thickness, and the presence of pinholes/pores in the SiO_2-shell can critically affect the selectivity and sensitivity of the sensor.[10b,13,15d] These aspects control the diffusion of gas molecules with respect to their size and nature, such as due to its smaller size (for example the molecular diameters of gases H_2, H_2O, O_2, and CO are reported as 2.18, 2.72, 2.96, and 3.80 Å, respectively)[15a] hydrogen can diffuse through the shell layer easier than the other analytes of interest.[28] Therefore, the diffusion of comparatively larger gas molecules such as acetone, ethanol, carbon monoxide, and hydrogen sulfide became negligible.[10b] Thus, the SiO_2-shell layer deposited on top of the SnO_2 NWs is mainly responsible for the selectivity towards hydrogen. Hydrogen (a reducing gas) is oxidized to water when it reacts with adsorbed oxygen species at the SnO_2 surface, accordingly narrowing the electron depletion region, Equations (3) and (4). This results in an increase in the width of the conduction channel and accordingly the conductance of the sensor increases (Scheme 2f). The higher sensing-response of SnO_2-SiO_2/20–60 CSNWs sensors than the bare-SnO_2 NWs is due to the greater width and a comparatively more resistive electron-depletion-layer.[15c,18b,22] Indeed, this highly resistive EDL increases the tendency of electron acceptance from hydrogen.[9b,15c,18b] However, with the increase of the shell thickness beyond a critical thickness (4.8 nm, in this study, cf. Figure 1g), the SiO_2 layer became too thick to allow for the diffusion of hydrogen molecules to the sensing layer and their oxidation products out, thereby it leads to a decrease of the sensor response (cf. the sensitivity of the SnO_2-SiO_2 /90 and SnO_2-SiO_2/130 CSNWs sensors in Figure 2g).[13]

3. Conclusion

In this article, we have investigated the gas-sensing properties and the underlying transduction mechanism of well-defined SnO_2-SiO_2 core-shell nanowires heterostructures with varying thickness of the amorphous SiO_2-shell layer (1.8–10.5 nm in thickness). The selectivity and response of pristine SnO_2 sensors are greatly enhanced by a conformal and homogeneous SiO_2 coating. The electrical properties and the sensor response of the SnO_2-SiO_2 core-shell nanowires heterostructures strongly depend on the thickness of the SiO_2 coatings. The SnO_2-SiO_2/60 CSNWs sensor with a SiO_2 film thickness of ca. 4.8 nm showed an optimized response of 160 (ca. seven-fold higher than pristine SnO_2 NWs) towards hydrogen (500 ppm) at 500 °C along with a lower detection limit of 0.1 ppm. This is attributed to an increase of the width of the electron-depletion-layer due to a strong core-shell coupling, where the conduction pathway is strictly confined to the SnO_2 core. In addition, an enhanced selectivity towards hydrogen is demonstrated due to a "masking effect" of the SiO_2 shell allowing hydrogen to more easily diffuse to the SnO_2 NWs surface compared to other reducing gases such as ethanol and carbon monoxide. The outstanding sensing properties of the SnO_2-SiO_2/*N* CSNWs can therefore be attributed to our heterostructured materials offering concurrently a high surface area, a homogeneous, conformal, and electronically coupled SiO_2 shell layer presenting an optimized thickness. All in all, because our study precisely correlates the structural characteristics of well-defined SnO_2-SiO_2 heterostructures to the gas-sensing properties, we anticipate that it will be helpful for the understanding and the application of next-generation gas-sensing material.

4. Experimental Section

Materials and Methods: (3-Aminopropyl)triethoxysilane, $((H_2N(CH_2)_3Si(OC_2H_5)_3$, APTES) and SnO_2 (99.9%) were acquired from Sigma-Aldrich. Ozone (O_3) was generated using oxygen (purity, 99.99%) in an ozone generator (BMT 803 N). Nitrogen, argon, and oxygen gases were supplied from Air Liquide (purity, 99.99%), and all of the certified gases for sensing tests were purchased by the SOL Group (Italy). Single-side polished (SSP) silicon-wafers (B014002) were purchased from Siegert wafer GmbH and used after cleaning in piranha solution.

Substrate Preparation and Growth of SnO_2 Nanowires: The substrate preparation was already reported in our earlier reports.[5,29] Briefly, an ultrathin layer of Au catalyst was deposited (onto the pre-cleaned alumina substrate, 2×2 mm^2) by a magnetron sputtering process (RF power = 50 W, argon mass flow = 7 sccm, pressure = approximately 5×10^{-3} mbar, time = 5 s) using a Kenotec Sputtering plant, Italy. SnO_2 NWs were produced directly onto the Au-catalyzed alumina substrates by VLS deposition in a custom designed tubular furnace (by Lenton) using SnO_2 powder. Au catalyzed substrates and SnO_2 powder contained in alumina crucibles were arranged into an alumina tube. The SnO_2 powder was placed in a relatively high temperature region (≈1370 °C) leading to its evaporation, whereas alumina substrates were placed in a comparatively colder-region (≈860 °C) to facilitate the condensation of the evaporated SnO_2 material. Argon (mass flow, 100 sccm) was applied as a carrier gas to facilitate the transport of the vapors from the SnO_2 source to the alumina substrates. The deposition time was set to 2 min.

Synthesis of SnO_2-SiO_2 Core–Shell Nanowires (CSNWs): Amorphous films of SiO_2 were directly deposited onto the SnO_2 nanowires (NWs) grown onto the alumina substrate, onto which the Pt-contacts were previously deposited (Scheme 1). The Pt-contacts were masked using a custom-made copper frame shadow mask. Pre-cleaned silicon-wafers were also coated simultaneously to the SnO_2 NWs to calibrate the thickness of the SiO_2 films by spectroscopic ellipsometry (SE). ALD was performed in a commercial ALD system (Arradiance, GEMStar-6). Before starting the ALD process, the ALD system was evacuated (≈8.6×10^{-3} mbar), and the temperature of the reaction chamber was stabilized at 160 °C. Prior to the ALD, all the samples were treated (in situ) with ozone to remove organic impurities (total exposure time, 300 s). The temperature of the ALD chamber and the supply lines was kept at 160 and 120 °C, respectively. APTES kept at 80 °C was used as Si precursor, whereas ozone and millipore water (kept at RT) were used as oxygen sources.[30] APTES, H_2O, and O_3 were introduced into the reaction chamber in a sequence using argon as a purging and a carrier gas. One ALD cycle was performed in a sequence of pulse/exposure/Ar-purge as 2 s/30 s/30 s, 0.2 s/30 s/40 s, and 0.2 s/30 s/40 s for APTES, H_2O, and O_3, respectively. The thickness of the SiO_2 film was controlled by changing the number of ALD cycles (20–130). The samples are named as SnO_2-SiO_2/*N*, where *N* represents the number of SiO_2 ALD cycles (i.e., 20, 40, 60, 90, and 130 ALD).

Morphological and Microstructural Characterization: The thickness of the SiO_2 film was initially estimated on silicon wafers by using a spectroscopic ellipsometer (SENTECH Instruments GmbH). The data was obtained at an incident angle of 70° for wavelengths ranging

370–1000 nm and an average of at least three measurements was considered. SAED, HAADF-STEM, BF-HRTEM, and EDX elemental mapping were acquired using a scanning/transmission electron microscope (S/TEM) operated at 200 kV (FEI Talos F200S). The TEM data including the SiO_2-shell thickness estimation directly onto the SnO_2 NWs were performed using Velox analytical software. SEMs were performed using a FEI Quanta 200 FEG microscope.

Fabrication of Sensing Device and Gas-Sensing Measurements: Six batches of gas-sensing devices were prepared including bare-SnO_2 NWs and SnO_2-SiO_2/*N* CSNWs with varying thicknesses of the SiO_2-shell layer (i.e., 1.8–10.5 nm). Prior to the SiO_2 ALD, two Pt-contacts in parallel positions were deposited onto the alumina substrate by a two-step deposition process. TiW alloy adhesion layers and Pt electrodes (thickness, ≈1 µm) were deposited by dc magnetron sputtering using 70 W argon plasma (≈0.55 Pa, rt.) with a deposition time of 3 and 20 min, respectively. The same two-step process was applied to deposit a micro-patterned platinum heater on the backside of alumina substrate using the same two-step process. Finally, all of the fabricated devices were mounted on the TO packages by electro-soldered gold wires.

Gas-Sensing measurements: A flow-through technique was used to analyze the sensing response in a customized stainless steel chamber placed inside a climate chamber (Angelantoni MTC 120, Italy) set at 20 °C. The temperature of the sensing-devices was controlled using a Thurlby Thandar Instruments Bench Power Supply (PL330DP). All the sensors were thermally stabilized for 8 h at the set temperature prior to the measurements in 0% and 40% relative humidity (RH% at 20 °C).

Analyte-gases with certified concentrations and dry air were mixed using mass flow controllers by MKS, Germany, where the total mass flow was maintained as 200 sccm. After the 30 min of exposure to a fixed concentration of the analyte, synthetic airflow was reestablished for 60 min to get a baseline recovery. A fixed voltage (1 V), using an Agilent E3631A power supply, was applied to the sensors and the electrical conductance of each of the sensor was recorded continuously by a picoammeters (Keithley 486, USA). The sensors response was determined by the variation in conductance/resistance using Equations (1) and (2) for oxidizing and reducing gases, respectively.

$$\text{Response}\,(S) = \frac{G_{\text{air}} - G_{\text{gas}}}{G_{\text{gas}}} = \frac{\Delta G}{G_{\text{gas}}} \tag{5}$$

$$\text{Response}\;\;(S) = \frac{G_{\text{gas}} - G_{\text{air}}}{G_{\text{air}}} = \frac{\Delta G}{G_{\text{air}}} \tag{6}$$

Where G_{air} and G_{gas} are the conductance of sensor in the synthetic air and in the target gas, respectively. The gas-sensing characteristics were studied for different concentrations of hydrogen and some interfering gases such as ethanol, acetone, carbon monoxide, and hydrogen sulfide. Initially, for all the sets of sensing devices, a temperature screening was performed between 200–500 °C to find the optimal working temperature. After the sensing parameters have been studied, the experimental data at optimal working temperature were fitted to a power-law (Equation (7)) for calibration curves (response versus hydrogen concentration).

$$\text{Response} = A[\text{Gas concentration}]^B \tag{7}$$

where *A* and *B* are the constants related to the material and the chemical reactions taking place at the surface, respectively.[5,29]

Supporting Information

Supporting Information is available from the Wiley Online Library or from the author.

Acknowledgements

The authors thankfully acknowledged C. Erdmann for electron microscopy measurements. They thank E. Wierzbicka for SEM measurements and J. Wang for assistance in some ALD experiments.

Open access funding enabled and organized by Projekt DEAL.

Conflict of Interest

The authors declare no conflict of interest.

Data Availability Statement

The data that support the findings of this study are available from the corresponding author upon reasonable request.

Keywords

atomic layer deposition, core-shell nanowires, H_2 selectivity, shell thickness, SnO_2-SiO_2

Received: June 9, 2021
Revised: June 22, 2021
Published online:

[1] Y. Liu, J. Parisi, X. Sun, Y. Lei, *J. Mater. Chem. A* **2014**, *2*, 9919.
[2] P. A. Russo, N. Donato, S. G. Leonardi, S. Baek, D. E. Conte, G. Neri, N. Pinna, *Angew. Chem., Int. Ed.* **2012**, *51*, 11053.
[3] a) T. Hübert, L. Boon-Brett, G. Black, U. Banach, *Sens. Actuators, B* **2011**, *157*, 329; b) S. M. Kim, H. J. Kim, H. J. Jung, J.-Y. Park, T. J. Seok, Y.-H. Choa, T. J. Park, S. W. Lee, *Adv. Funct. Mater.* **2019**, *29*, 1807760.
[4] a) G. Sberveglieri, C. Baratto, E. Comini, G. Faglia, M. Ferroni, M. Pardo, A. Ponzoni, A. Vomiero, *Thin Solid Films* **2009**, *517*, 6156; b) M. Sitarz, M. Kwoka, E. Comini, D. Zappa, J. Szuber, *Nanoscale Res. Lett.* **2014**, *9*, 43.
[5] M. H. Raza, N. Kaur, E. Comini, N. Pinna, *ACS Appl. Mater. Interfaces* **2020**, *12*, 4594.
[6] V. K. K. Tangirala, H. Gómez-Pozos, V. Rodríguez-Lugo, M. D. L. L. Olvera, *Sensors* **2017**, *17*, 1011.
[7] a) M. Kwoka, B. Lyson-Sypien, A. Kulis, D. Zappa, E. Comini, *Nanomaterials* **2018**, *8*, 738; b) D. D. Trung, N. D. Hoa, P. V. Tong, N. V. Duy, T. D. Dao, H. V. Chung, T. Nagao, N. V. Hieu, *J. Hazard. Mater.* **2014**, *265*, 124; c) M. Zhuo, Y. Chen, J. Sun, H. Zhang, D. Guo, H. Zhang, Q. Li, T. Wang, Q. Wan, *Sens. Actuators, B* **2013**, *186*, 78.
[8] a) A. Vomiero, M. Ferroni, E. Comini, G. Faglia, G. Sberveglieri, *Nano Lett.* **2007**, *7*, 3553; b) S. Lettieri, A. Bismuto, P. Maddalena, C. Baratto, E. Comini, G. Faglia, G. Sberveglieri, L. Zanotti, *J. Non-Cryst. Solids* **2006**, *352*, 1457.
[9] a) S. Park, H. Ko, S. Kim, C. Lee, *ACS Appl. Mater. Interfaces* **2014**, *6*, 9595; b) D. Degler, U. Weimar, N. Barsan, *ACS Sens.* **2019**, *4*, 2228; c) M. H. Raza, K. Movlaee, S. G. Leonardi, N. Barsan, G. Neri, N. Pinna, *Adv. Funct. Mater.* **2020**, *30*, 1906874.
[10] a) C. Cheng, T.-L. Wang, L. Feng, W. Li, K. M. Ho, M. M. T. Loy, K. K. Fung, N. Wang, *Nanotechnology* **2010**, *21*, 475703; b) G. Tournier, C. Pijolat, *Sens. Actuators, B* **2005**, *106*, 553.
[11] a) A. Ryzhikov, M. Labeau, A. Gaskov, *Sens. Actuators, B* **2005**, *109*, 91; b) M. Weber, J.-Y. Kim, J.-H. Lee, J.-H. Kim, I. Iatsunskyi,

E. Coy, P. Miele, M. Bechelany, S. S. Kim, *J. Mater. Chem. A* **2019**, *7*, 8107.

[12] a) M. Weber, J.-H. Kim, J.-H. Lee, J.-Y. Kim, I. Iatsunskyi, E. Coy, M. Drobek, A. Julbe, M. Bechelany, S. S. Kim, *ACS Appl. Mater. Interfaces* **2018**, *10*, 34765; b) M. I. Nandasiri, S. R. Jambovane, B. P. McGrail, H. T. Schaef, S. K. Nune, *Coord. Chem. Rev.* **2016**, *311*, 38.

[13] J. van den Broek, I. C. Weber, A. T. Güntner, S. E. Pratsinis, *Mater. Horiz.* **2021**, *8*, 661.

[14] X. Meng, Q. Zhang, S. Zhang, Z. He, *Sensors* **2019**, *19*, 2478.

[15] a) A. Katsuki, K. Fukui, *Sens. Actuators, B* **1998**, *52*, 30; b) K. Wada, M. Egashira, *Sens. Actuators, B* **2000**, *62*, 211; c) K. Wada, M. Egashira, *Sens. Actuators, B* **1998**, *53*, 147; d) S. Gunji, M. Jukei, Y. Shimotsuma, K. Miura, K. Suematsu, K. Watanabe, K. Shimanoe, *J. Mater. Chem. C* **2017**, *5*, 6369.

[16] D. R. Miller, S. A. Akbar, P. A. Morris, *Sens. Actuators, B* **2014**, *204*, 250.

[17] a) E. Comini, C. Baratto, G. Faglia, M. Ferroni, A. Vomiero, G. Sberveglieri, *Prog. Mater. Sci.* **2009**, *54*, 1; b) N. Kaur, E. Comini, D. Zappa, N. Poli, G. Sberveglieri, *Nanotechnology* **2016**, *27*, 205701.

[18] a) N. Kaur, M. Singh, E. Comini, *Langmuir* **2020**, *36*, 6326; b) M. Singh, N. Kaur, G. Drera, A. Casotto, L. Sangaletti, E. Comini, *Adv. Funct. Mater.* **2020**, *30*, 2003217; c) E. Comini, G. Faglia, M. Ferroni, A. Ponzoni, A. Vomiero, G. Sberveglieri, *J. Mol. Catal. A: Chem.* **2009**, *305*, 170; d) C. Marichy, P. A. Russo, M. Latino, J.-P. Tessonnier, M.-G. Willinger, N. Donato, G. Neri, N. Pinna, *J. Phys. Chem. C* **2013**, *117*, 19729; e) J. M. Ziegler, I. Andoni, E. J. Choi, L. Fang, H. Flores-Zuleta, N. J. Humphrey, D.-H. Kim, J. Shin, H. Youn, R. M. Penner, *Anal. Chem.* **2021**, *93*, 124.

[19] a) C. Marichy, A. Pucci, M.-G. Willinger, N. Pinna, in *Atomic Layer Deposition of Nanostructured Materials*, (Eds: N. Pinna, M. Knez), Wiley-VCH, Weinheim **2012**, p. 327; b) C. Marichy, M. Bechelany, N. Pinna, *Adv. Mater.* **2012**, *24*, 1017; c) C. Marichy, N. Pinna, *Adv. Mater. Interfaces* **2016**, *3*, 1600335.

[20] a) A. Ponti, M. H. Raza, F. Pantò, A. M. Ferretti, C. Triolo, S. Patanè, N. Pinna, S. Santangelo, *Langmuir* **2020**, *36*, 1305; b) M. H. Raza, K. Movlaee, Y. Wu, S. M. El-Refaei, M. Karg, S. G. Leonardi, G. Neri, N. Pinna, *ChemElectroChem* **2019**, *6*, 383; c) Y. Wu, M. H. Raza, Y.-C. Chen, P. Amsalem, S. Wahl, K. Skrodczky, X. Xu, K. S. Lokare, M. Zhukush, P. Gaval, N. Koch, E. A. Quadrelli, N. Pinna, *Chem. Mater.* **2019**, *6*, 1881.

[21] a) A. Staerz, Y. Liu, U. Geyik, H. Brinkmann, U. Weimar, T. Zhang, N. Barsan, *Sens. Actuators, B* **2019**, *291*, 378; b) A. Staerz, T.-H. Kim, J.-H. Lee, U. Weimar, N. Barsan, *J. Phys. Chem. C* **2017**, *121*, 24701.

[22] W. Liu, L. Xu, K. Sheng, C. Chen, X. Zhou, B. Dong, X. Bai, S. Zhang, G. Lu, H. Song, *J. Mater. Chem. A* **2018**, *6*, 10976.

[23] a) Y. Liang, C. Tracy, E. Weisbrod, P. Fejes, N. D. Theodore, *Appl. Phys. Lett.* **2006**, *88*, 081901; b) V. V. Afanas'ev, *Adv. Condens. Matter Phys.* **2014**, *2014*, 301302; c) M. S. Choi, H. G. Na, J. H. Bang, A. Mirzaei, S. Han, H. Y. Lee, S. S. Kim, H. W. Kim, C. Jin, *Sens. Actuators, B* **2021**, *326*, 128801.

[24] J. Hu, J. Yang, W. Wang, Y. Xue, Y. Sun, P. Li, K. Lian, W. Zhang, L. Chen, J. Shi, Y. Chen, *Mater. Res. Bull.* **2018**, *102*, 294.

[25] E. Comini, *Anal. Chim. Acta* **2006**, *568*, 28.

[26] N. Barsan, U. Weimar, *J. Electroceram.* **2001**, *7*, 143.

[27] E. Comini, *Mater. Today Adv.* **2020**, *7*, 100099.

[28] C. D. Feng, Y. Shimizu, M. Egashira, *J. Electrochem. Soc.* **1994**, *141*, 220.

[29] N. Kaur, D. Zappa, M. Ferroni, N. Poli, M. Campanini, R. Negrea, E. Comini, *Sens. Actuators, B* **2018**, *262*, 477.

[30] J. Bachmann, R. Zierold, Y. T. Chong, R. Hauert, C. Sturm, R. Schmidt-Grund, B. Rheinländer, M. Grundmann, U. Gösele, K. Nielsch, *Angew. Chem., Int. Ed.* **2008**, *47*, 6177.